Acta Mech. Sin. (2017) 33(4):733–741
DOI 10.1007/s10409-017-0695-2

RESEARCH PAPER

A gas-kinetic theory based multidimensional high-order method for the compressible Navier–Stokes solutions

Xiaodong Ren[1] · **Kun Xu**[2,3] · **Wei Shyy**[3]

Received: 22 February 2017 / Revised: 6 May 2017 / Accepted: 12 May 2017 / Published online: 20 June 2017
© The Chinese Society of Theoretical and Applied Mechanics; Institute of Mechanics, Chinese Academy of Sciences and Springer-Verlag Berlin Heidelberg 2017

Abstract This paper presents a gas-kinetic theory based multidimensional high-order method for the compressible Naiver–Stokes solutions. In our previous study, a spatially and temporally dependent third-order flux scheme with the use of a third-order gas distribution function is employed. However, the third-order flux scheme is quite complicated and less robust than the second-order scheme. In order to reduce its complexity and improve its robustness, the second-order flux scheme is adopted instead in this paper, while the temporal order of method is maintained by using a two stage temporal discretization. In addition, its CPU cost is relatively lower than the previous scheme. Several test cases in two and three dimensions, containing high Mach number compressible flows and low speed high Reynolds number laminar flows, are presented to demonstrate the method capacity.

Keywords Discontinuous Galerkin · Two-stage temporal discretization · Gas-kinetic theory

✉ Kun Xu
makxu@ust.hk

[1] Key Laboratory for Thermal Science and Power Engineering of Ministry of Education, Department of Thermal Engineering, Tsinghua University, Beijing 100084, China

[2] Department of Mathematics, School of Science, The Hong Kong University of Science and Technology, Hong Kong, China

[3] Department of Mechanical and Aerospace Engineering, School of Engineering, The Hong Kong University of Science and Technology, Hong Kong, China

1 Introduction

Although the second-order numerical methods are still widely used, high-order methods (higher than second-order) have been given more and more attention due to the low dissipation and high resolution. Generally, for a finite volume method (FVM), a large stencil is often used to achieve high-order accuracy. These methods are effective for structure meshes, but may face problems on arbitrary grids due to difficulties building a large stencil and the parallel communication. To deal with these difficulties, a compact method is the first choice and the discontinuous Galerkin method (DGM) [1] can satisfy the request. The DGM uses the higher-order polynomial approximation inside each cell to obtain a higher-order accuracy. The adjacent cells information is only needed to update the degrees of freedom. Thus, the DGM is very compact and easy to be applied. At the beginning, the DGM is introduced for the linear transport equations [2,3]. Then, Chavent and Salzano [4] applied it to the nonlinear case. However, the original method is unstable for the nonlinear case, and thus Cockburn and Shu [1,5] further developed the method using the multi-step Runge–Kutta method to solve the nonlinear time-dependent hyperbolic conservation laws. For the Navier–Stokes (NS) equations, the DGM [1,5] cannot be applied due to the non-conforming problem [6]. In order to apply the DGM to the viscous case, Bassi and Rebay [7] firstly introduce auxiliary variables and the NS equations are rewritten into a first-order system. Then, this idea is further analyzed, and the local discontinuous Galerkin method (LDGM) is proposed [8]. One should note that the Riemann solver or approximate Riemann solver is always employed to estimate the inviscid flux, while the viscous term is treated in a different way. Actually, the Riemann solver just has first-order accuracy and the flux evaluation may have large error.

In addition, the Riemann solver may lead to shock instability, and some cures should be employed [9–12]. To improve the accuracy of the method, we will use a high-order approximate polynomial, as well as improve the accuracy of the flux evaluation. Meanwhile, the method will not have the shock instability.

Fortunately, a second-order FVM based on the gas-kinetic theory [13] has been proposed, and the shock instability is avoided. In the gas-kinetic FVM, the flux function is constructed based on the integral solution of the gas-kinetic Bhatnagar–Gross–Krook (BGK) model. It contains both inviscid and viscous terms and presents a multiscale evolution process from a non-equilibrium to an equilibrium state. The time evolution of both flow variables and their derivatives is considered, which means the flux evaluation has a high-order accuracy. Therefore, it is a better choice to develop a DGM based on the gas-kinetic theory. The work by Xu [14] firstly proposed a 1D DGM by using a second-order gas-kinetic flux scheme. Then Liu and Xu [15] also used a second-order gas-kinetic flux scheme while the directional splitting method is employed for the 2D cases. Works by Ni et al. [16] and Luo et al. [17] also used the second-order BGK scheme for the flux evaluation. The study by Ren et al. [18] developed a third-order gas-kinetic DGM, in which a multi-dimensional third-order gas-kinetic flux scheme is employed.

However, the third-order gas-kinetic flux scheme is quite complicated, in which both the first-order and the second-order derivatives of the flow variables are considered, and it is very difficult for engineers to learn and use it. In addition, due to the second-order derivatives, the third-order scheme is more sensitive to the grid quality and flow condition, especially for the problems with a moving mesh. If there is a strong discontinuity, more attention should be paid to the second-order derivatives to prevent oscillation. In summary, its robustness is lower than the second-order scheme, and its applications are very careful in the real engineering. In order to overcome this problem, the second-order flux scheme is adopted instead in this paper, while the time accuracy is maintained by using a two-stage temporal discretization [19]. Furthermore, the CPU cost is relatively lower than the previous scheme.

This paper is organized as follows. Section 2 is the construction of the gas kinetic theory based discontinuous Galerkin method with the two-stage temporal discretization. Section 3 shows some numerical examples and the results. The last section draws the conclusion.

2 Gas kinetic theory based discontinuous Galerkin method with a two-stage temporal discretization

The 3D gas-kinetic BGK model can be written as

$$\frac{\partial f}{\partial t} + \boldsymbol{u} \cdot \nabla f = \frac{g - f}{\tau}, \tag{1}$$

where f is the gas distribution function of the physical time t, $\boldsymbol{u} = (u, v, w)$ is the particle velocity vector, ∇f is the gradient of f with respect to $\boldsymbol{x} = (x, y, z)$, g is the equilibrium state approached by f, and τ is the particle collision time relating to the viscosity and heat conduction coefficients.

The equilibrium state is a Maxwellian distribution,

$$g = \rho \left(\frac{\lambda}{\pi}\right)^{\frac{K+3}{2}} \mathrm{e}^{-\lambda\left[(u-U)^2 + (v-V)^2 + (w-W)^2 + \xi^2\right]}, \tag{2}$$

in which ρ is the density, U, V, and W are the macroscopic velocity in x, y, and z directions, and $\lambda = m/(2kT)$ is related to the gas temperature T, with m being the molecular mass and k the Boltzmann constant. $K = (5 - 3\gamma)/(\gamma - 1)$ is the total number of degrees of freedom in the internal variable ξ, and γ is the specific heat ratio. For the equilibrium state g, $\xi^2 = \xi_1^2 + \xi_2^2 + \cdots + \xi_K^2$. Equation (3) shows the connection between the macroscopic conservative variables $\boldsymbol{Q}$ and the distribution function f

$$\boldsymbol{Q} = (\rho, \rho U, \rho V, \rho W, \rho E)^{\mathrm{T}} = \int \boldsymbol{\psi} f \mathrm{d}\boldsymbol{\Xi} = \int \boldsymbol{\psi} g \mathrm{d}\boldsymbol{\Xi}, \tag{3}$$

where the vector of moments $\boldsymbol{\psi}$ is

$$\boldsymbol{\psi} = \left[1, u, v, w, \frac{1}{2}\left(u^2 + v^2 + w^2 + \xi^2\right)\right]^{\mathrm{T}}, \tag{4}$$

and $\mathrm{d}\boldsymbol{\Xi} = \mathrm{d}u\mathrm{d}v\mathrm{d}w\mathrm{d}\xi_1\mathrm{d}\xi_2 \cdots \mathrm{d}\xi_K$ is the volume element in the phase space.

Since the mass, momentum, and energy are conserved during particle collisions, f and g satisfy the conservation constraint at any point in space and time,

$$\int \boldsymbol{\psi} \frac{g - f}{\tau} \mathrm{d}\boldsymbol{\Xi} = 0, \tag{5}$$

where τ depends on macroscopic variables and is independent of particle velocity.

To obtain the NS solution, the Chapman–Enskog expansion in Eq. (6) is adopted [13],

$$f_{\mathrm{NS}}(\boldsymbol{x}, t, u, v, w, \xi) = g - \tau\left(\frac{\partial g}{\partial t} + u\frac{\partial g}{\partial x} + v\frac{\partial g}{\partial y} + w\frac{\partial g}{\partial z}\right). \tag{6}$$

The relation between the flux and the distribution function is as follows

$$\boldsymbol{F} = \int \boldsymbol{u}\boldsymbol{\psi} f \mathrm{d}\boldsymbol{\Xi}. \tag{7}$$

Based on Eqs. (3) and (7), we have

$$\frac{\partial \boldsymbol{Q}(\boldsymbol{x}, t)}{\partial t} + \nabla \cdot F = 0, \quad \boldsymbol{x} \in \Omega, \tag{8}$$

where Ω indicates the flow domain. Note that Eq. (8) describes a general conservation law, which does not imply the equilibrium limit ($\tau \to 0$), i.e. $f = g$ for the Euler equations. The zero on the right side is due to the conservation property in Eq. (5), which is valid for the update of conservative variables.

In order to obtain the numerical approximate solution of $\boldsymbol{Q}$, the domain Ω is decomposed into a finite number of cells and expressed as

$$\Omega \doteq \bigcup_{e=1}^{m} \Omega_e = \{\Omega_1, \Omega_2, \ldots, \Omega_m\}, \quad m \in \mathbb{N}, \tag{9}$$

where m is the total number of the mesh elements.

A local polynomial basis $\{\upsilon_0 = 1, \upsilon_1', \ldots, \upsilon_{l-1}'\}$ is adopted to define the approximate polynomial solution in each cell

$$\boldsymbol{Q} \doteq \boldsymbol{Q}_h(x, t) = \bar{\boldsymbol{Q}}(t) + \sum_{i=1}^{l-1} \hat{\boldsymbol{Q}}_i(t)\left[\upsilon_i'(x) - \bar{\upsilon}_i'\right], \quad \boldsymbol{x} \in \Omega_e,\ t \geqslant 0, \quad l \in \mathbb{N}, \tag{10}$$

in which l is the number of the basis function, $\bar{\boldsymbol{Q}}(t)$ is the cell mean value of the conservative variable, and $\bar{\upsilon}_i'$ is the cell mean value of the basis function within the cell, which has the following definition

$$\bar{\upsilon}_i' = \frac{1}{|\Omega_e|}\int_{\Omega_e} \upsilon_i' \mathrm{d}\boldsymbol{x}, \tag{11}$$

where $|\Omega_e|$ is the cell volume.

Rewrite the basis functions as $\upsilon_i = \upsilon_i' - \bar{\upsilon}_i'$ and Eq. (10) can be rewritten as

$$\boldsymbol{Q}_h(\boldsymbol{x}, t) = \bar{\boldsymbol{Q}}(t) + \sum_{i=1}^{l-1} \hat{\boldsymbol{Q}}_i(t)\upsilon_i(\boldsymbol{x}). \tag{12}$$

Although different basis functions can be used for the DGM, a Taylor series expansion [20] at the cell center is employed in this paper, which can be applied on arbitrary grids. The cell mean values of the conservative variables are updated by using the two-stage temporal discretization as follows

$$\left(\bar{\boldsymbol{Q}}\right)^{*} = \left(\bar{\boldsymbol{Q}}\right)^{n} - \frac{1}{|\Omega_e|}\int_{\partial\Omega_e}\int_{t^n}^{t^n+\frac{1}{2}\Delta t} \boldsymbol{F}\left(\boldsymbol{Q}^n, t\right)\mathrm{d}t \cdot \boldsymbol{n}\mathrm{d}S, \tag{13}$$

$$\begin{aligned}\left(\bar{\boldsymbol{Q}}\right)^{n+1} = \left(\bar{\boldsymbol{Q}}\right)^{n} - \frac{1}{|\Omega_e|}\int_{\partial\Omega_e}\Bigg[&\frac{8}{3}\int_{t^n}^{t^n+\frac{1}{2}\Delta t} \boldsymbol{F}\left(\boldsymbol{Q}^n, t\right)\mathrm{d}t \\ &- \frac{1}{3}\int_{t^n}^{t^n+\Delta t} \boldsymbol{F}\left(\boldsymbol{Q}^n, t\right)\mathrm{d}t\Bigg] \cdot \boldsymbol{n}\mathrm{d}S \\ - \frac{1}{|\Omega_e|}\int_{\partial\Omega_e}\Bigg[&\frac{4}{3}\int_{t^n}^{t^*+\Delta t} \boldsymbol{F}\left(\boldsymbol{Q}^*, t\right)\mathrm{d}t \\ &- \frac{8}{3}\int_{t^n}^{t^*+\frac{1}{2}\Delta t} \boldsymbol{F}\left(\boldsymbol{Q}^*, t\right)\mathrm{d}t\Bigg] \cdot \boldsymbol{n}\mathrm{d}S,\end{aligned} \tag{14}$$

where $\partial\Omega_e$ indicates the interface, $\boldsymbol{n}$ is its outward normal unit-vector, $t^* = t^n + \Delta t/2$ is an intermediate time, and Δt is the time step.

For other degrees of freedom, the DGM is used, as shown in Eq. (15)

$$\begin{aligned}&\int_{\Omega_e} \frac{\partial\left[\bar{\boldsymbol{Q}}(t) + \sum_{i=1}^{l-1}\hat{\boldsymbol{Q}}_i(t)\upsilon_i(\boldsymbol{x})\right]}{\partial t}\upsilon_j(\boldsymbol{x})\mathrm{d}\boldsymbol{x} \\ &\quad + \int_{\Omega_e} \nabla \cdot \boldsymbol{F}\upsilon_j(\boldsymbol{x})\mathrm{d}\boldsymbol{x} = 0, \qquad j = 1, 2, \ldots, l-1.\end{aligned} \tag{15}$$

And Eq. (15) can be rewritten as

$$\begin{aligned}\sum_{i=1}^{l-1}\overline{\upsilon_i\upsilon_j}\frac{\partial\hat{\boldsymbol{Q}}_i}{\partial t} &= \frac{1}{|\Omega_e|}\int_{\Omega_e} \boldsymbol{F}\cdot\nabla\upsilon_j(\boldsymbol{x})\mathrm{d}\boldsymbol{x} \\ &\quad - \frac{1}{|\Omega_e|}\int_{\partial\Omega_e} \boldsymbol{F}\cdot\boldsymbol{n}\upsilon_j(\boldsymbol{x})\mathrm{d}S, \quad j = 1, 2, \ldots, l-1,\end{aligned} \tag{16}$$

where $\overline{\upsilon_i\upsilon_j} = \frac{1}{|\Omega_e|}\int_{\Omega_e}\upsilon_i(\boldsymbol{x})\upsilon_j(\boldsymbol{x})\mathrm{d}\boldsymbol{x}$.

Again the two stage temporal discretization is used, and we have

$$\begin{aligned}\sum_{i=1}^{l-1}\overline{\upsilon_i\upsilon_j}\left(\hat{\boldsymbol{Q}}_i^{*} - \hat{\boldsymbol{Q}}_i^{n}\right) &= \frac{1}{|\Omega_e|}\int_{\Omega_e}\int_{t^n}^{t^n+\frac{1}{2}\Delta t} \boldsymbol{F}\left(\boldsymbol{Q}^n, t\right)\mathrm{d}t \\ &\quad \cdot\nabla\upsilon_j(\boldsymbol{x})\mathrm{d}\boldsymbol{x}\end{aligned}$$

$$-\frac{1}{|\Omega_e|}\int_{\partial\Omega_e}\int_{t^n}^{t^n+\frac{1}{2}\Delta t}\boldsymbol{F}\left(\boldsymbol{Q}^n,t\right)\mathrm{d}t\cdot\boldsymbol{n}\upsilon_j\left(\boldsymbol{x}\right)\mathrm{d}S, \tag{17}$$

$$\sum_{i=1}^{l-1}\overline{\upsilon_i\upsilon_j}\left(\hat{\boldsymbol{Q}}_i^{n+1}-\hat{\boldsymbol{Q}}_i^n\right)=\frac{1}{|\Omega_e|}\times\int_{\Omega_e}\left[\frac{8}{3}\int_{t^n}^{t^n+\frac{1}{2}\Delta t}\boldsymbol{F}\left(\boldsymbol{Q}^n,t\right)\mathrm{d}t-\frac{1}{3}\int_{t^n}^{t^n+\Delta t}\boldsymbol{F}\left(\boldsymbol{Q}^n,t\right)\mathrm{d}t\right]\cdot\nabla\upsilon_j\left(\boldsymbol{x}\right)\mathrm{d}\boldsymbol{x}$$
$$-\frac{1}{|\Omega_e|}\int_{\partial\Omega_e}\left[\frac{8}{3}\int_{t^n}^{t^n+\frac{1}{2}\Delta t}\boldsymbol{F}\left(\boldsymbol{Q}^n,t\right)\mathrm{d}t-\frac{1}{3}\int_{t^n}^{t^n+\Delta t}\boldsymbol{F}\left(\boldsymbol{Q}^n,t\right)\mathrm{d}t\right]\cdot\boldsymbol{n}\upsilon_j\left(\boldsymbol{x}\right)\mathrm{d}S$$
$$+\frac{1}{|\Omega_e|}\int_{\Omega_e}\left[\frac{4}{3}\int_{t^*}^{t^*+\Delta t}\boldsymbol{F}\left(\boldsymbol{Q}^*,t\right)\mathrm{d}t-\frac{8}{3}\int_{t^*}^{t^*+\frac{1}{2}\Delta t}\boldsymbol{F}\left(\boldsymbol{Q}^*,t\right)\mathrm{d}t\right]\cdot\nabla\upsilon_j\left(\boldsymbol{x}\right)\mathrm{d}\boldsymbol{x}$$
$$-\frac{1}{|\Omega_e|}\int_{\partial\Omega_e}\left[\frac{4}{3}\int_{t^*}^{t^*+\Delta t}\boldsymbol{F}\left(\boldsymbol{Q}^*,t\right)\mathrm{d}t-\frac{8}{3}\int_{t^*}^{t^*+\frac{1}{2}\Delta t}\boldsymbol{F}\left(\boldsymbol{Q}^*,t\right)\mathrm{d}t\right]\cdot\boldsymbol{n}\upsilon_j\left(\boldsymbol{x}\right)\mathrm{d}S. \tag{18}$$

To prevent the oscillation around the discontinuity, a compact limiter with a shock detector [18] is adopted in this paper. A second-order gas-kinetic flux scheme is adopted to evaluate the fluxes.

In our previous study [18], a third-order flux scheme is employed to estimate both volume and interface fluxes. Both the first and second-order derivatives of the conservative variables are needed, thus, it is quite complex and expensive. And its robustness is lower than the second-order scheme. In order to overcome this problem, a second-order flux scheme is adopted instead here, and Gauss quadrature is used for all the spatial integrations. The gas distribution function for each Gauss quadrature point will be present in the following.

The conservative variable in each cell is assumed to be smooth and it is updated automatically based on Eqs. (13), (14), (17), and (18). The time-dependent gas distribution function on i-th Gauss quadrature point $\boldsymbol{x}_i$ in a cell can be expressed as

$$f\left(\boldsymbol{x}_i,t-t^n,u,v,w,\xi\right)=g^n-\tau\left(ua_x^n+va_y^n+wa_z^n\right)g^n+\left(t-t^n-\tau\right)A_t^n g^n, \tag{19}$$

with the notations

$$g^n=g\left(x_i,y_i,z_i,0,u,v,w,\xi\right),$$
$$a_x^n=\frac{1}{g^n}\frac{\partial g^n}{\partial x},\quad a_y^n=\frac{1}{g^n}\frac{\partial g^n}{\partial y},\quad a_z^n=\frac{1}{g^n}\frac{\partial g^n}{\partial z},$$
$$A_t^n=\frac{1}{g^n}\frac{\partial g^n}{\partial t}.$$

The physical collision time τ is related to the dynamical viscosity coefficient μ and the pressure p on i-th Gauss quadrature point

$$\tau=\frac{\mu}{p}. \tag{20}$$

In the above formulations, the equilibrium state g^n is determined from the conservative flow variables on i-th Gauss quadrature point at time n and the other expansion coefficient ϕ can be always written as follows [13]

$$\phi=\phi_1+\phi_2u+\phi_3v+\phi_4w+\frac{1}{2}\phi_5\left(u^2+v^2+w^2+\xi^2\right)=\left(\phi_1,\phi_2,\phi_3,\phi_4,\phi_5\right)\cdot\boldsymbol{\psi}. \tag{21}$$

Introducing the following notation

$$\langle\cdots\rangle=\int g^n\left(\cdots\right)\boldsymbol{\psi}\mathrm{d}\boldsymbol{\Xi}, \tag{22}$$

and all unknowns can be calculated using the following equations, which are based on Eq. (5)

$$\left\langle a_x^n\right\rangle=\frac{\partial\boldsymbol{Q}\left(x_i,0\right)}{\partial x}\rightarrow\left(a_{x,1}^n,a_{x,2}^n,a_{x,3}^n,a_{x,4}^n,a_{x,5}^n\right),$$
$$\left\langle a_y^n\right\rangle=\frac{\partial\boldsymbol{Q}\left(x_i,0\right)}{\partial y}\rightarrow\left(a_{y,1}^n,a_{y,2}^n,a_{y,3}^n,a_{y,4}^n,a_{y,5}^n\right),$$
$$\left\langle a_z^n\right\rangle=\frac{\partial Q\left(x_i,0\right)}{\partial z}\rightarrow\left(a_{z,1}^n,a_{z,2}^n,a_{z,3}^n,a_{z,4}^n,a_{z,5}^n\right),$$
$$\left\langle ua_x^n+va_y^n+wa_z^n+A_t^n\right\rangle=0\rightarrow\left(A_{t,1}^n,A_{t,2}^n,A_{t,3}^n,A_{t,4}^n,A_{t,5}^n\right).$$

At the cell interface, generally, a discontinuous initial condition appears, which corresponds to the non-equilibrium state around the cell interface. A smooth continuous equilibrium state will be achieved from the initial non-equilibrium state through the gas particle collision, and the equilibrium state can be constructed by using a local linear least square method as shown in Ref. [18]. The time dependent gas distribution

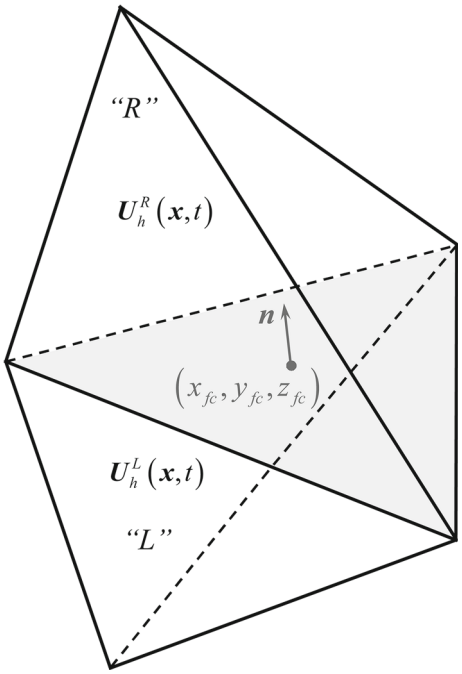

Fig. 1 A cell interface sketch

function on i-th Gauss quadrature point $\boldsymbol{x}_i$ on the cell interface can be expressed as

$$f\left(\boldsymbol{x}_i, t-t^n, u, v, w, \xi\right) = \left[1-\mathrm{e}^{-(t-t^n)/\tau_n}\right] g^n + \mathrm{e}^{-(t-t^n)/\tau_n} \times \left\{g^{n,R}\left[1-\mathrm{H}\left(u_n\right)\right] + g^{n,L}\mathrm{H}\left(u_n\right)\right\} - \tau\left(ua_x^n + va_y^n + wa_z^n\right) g^n + \left(t-t^n-\tau\right) A_t^n g^n, \quad (23)$$

where $\mathrm{H}(x)$ is the Heaviside function defined as

$$\mathrm{H}\left(x\right) = \begin{cases} 0, & x < 0, \\ 1, & x > 0, \end{cases} \quad (24)$$

and $u_n = \boldsymbol{u}\cdot\boldsymbol{n}$ is the normal component of the velocity on the interface, "R" means right side of the interface, and "L" means the left side of the interface, as shown in Fig. 1.

Similar to the method shown in Ref. [18], based on the initial conditions at the left and right sides of a cell interface, which are given by the DGM initially, the gas distribution function on i-th Gauss quadrature point $\boldsymbol{x}_i$ can be uniquely determined, and then the interface flux can be estimated.

Here two collision times [21] τ and τ_n are used. The physical collision time is shown in Eq. (20). The numerical collision time τ_n controls the contributions from f_0 and g in the final integral solution in the discontinuous case. Therefore, the numerical collision time τ_n is modeled with the consideration of the cell size and artificial discontinuous jump

$$\tau_n = \frac{\mu}{p} + \beta\left|\left(\boldsymbol{x}_c^R - \boldsymbol{x}_c^L\right)\cdot\boldsymbol{n}\right|\sqrt{\lambda}\frac{\left|p^R - p^L\right|}{\left|p^R + p^L\right|}, \quad (25)$$

in which $\boldsymbol{x}_c^R$ and $\boldsymbol{x}_c^L$ indicate the left and right cell barycenters. β is a constant and the proposed value is 0.0001–0.1. For a smooth flow case, a small value can be considered, while a large value should be used for a case with discontinuity.

3 Numerical examples

3.1 Taylor vortex problem

The Taylor vortex problem is used for the accuracy test and was used in Ref. [22]. The computational domain Ω is $[0, 1] \times [0, 1] \times [0, 0.1] \subset \mathbb{R}^3$ and the exact solution is

$$\begin{aligned} &\rho\left(x, y, z, t\right) = 1.0, \\ &U\left(x, y, z, t\right) = -\tfrac{1}{2\pi}\cos\left(2\pi x\right)\sin\left(2\pi y\right)\mathrm{e}^{-8\pi^2\nu t}, \\ &V\left(x, y, z, t\right) = \tfrac{1}{2\pi}\sin\left(2\pi x\right)\cos\left(2\pi y\right)\mathrm{e}^{-8\pi^2\nu t}, \\ &W\left(x, y, z, t\right) = 0, \\ &p\left(x, y, z, t\right) = 1 - \tfrac{1}{4}\left[\tfrac{\cos(4\pi x)}{4\pi^2} + \tfrac{\cos(4\pi y)}{4\pi^2}\right]\mathrm{e}^{-16\pi^2\nu t}, \end{aligned} \quad (26)$$

where the shear viscosity $\nu = 0.001$.

When the time $t = 0.0$, Eq. (26) is the initial condition for the simulation. In both x and y directions, a periodic condition is applied, while a symmetric condition is imposed on the plane in z direction. One should note that, due to the consideration of the energy equation, an additional source term is added to the energy equation to keep the energy conservation. A simple grid with mesh size $h = 0.1$ is shown in Fig. 2, and it can be seen that only one layer in z direction is used. To test

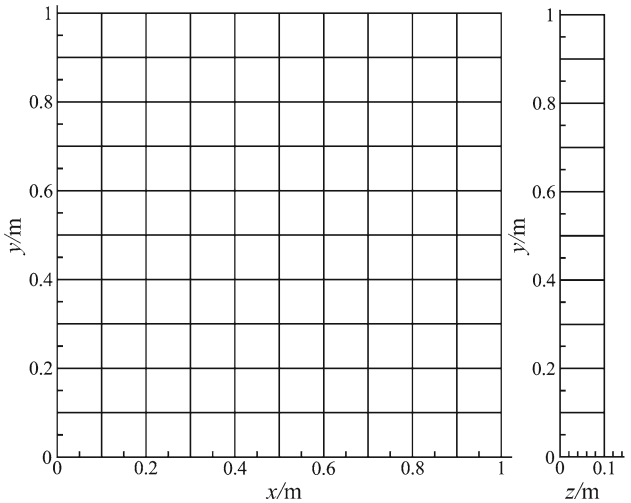

Fig. 2 The sample grid with ten cells in x and y directions, and one cell in z direction

Table 1 L^1 errors and L^∞ errors of U velocity and pressure

h	U velocity				p			
	L^1error	L^∞error	L^1order	L^∞order	L^1error	L^∞error	L^1order	L^∞order
0.10000	8.18×10^{-7}	1.89×10^{-6}	–	–	2.03×10^{-6}	3.09×10^{-6}	–	–
0.05000	1.13×10^{-7}	2.56×10^{-7}	2.85	2.88	2.72×10^{-7}	4.73×10^{-7}	2.90	2.71
0.02500	1.56×10^{-8}	3.73×10^{-8}	2.86	2.78	3.81×10^{-8}	6.52×10^{-8}	2.84	2.86
0.01250	2.33×10^{-9}	6.08×10^{-9}	2.74	2.62	5.85×10^{-9}	1.03×10^{-8}	2.70	2.66

the accuracy, the mesh is refined in the $x - y$ plane by quartering all the cells. The mesh sizes are shown in Table 1 with the errors of the pressure and U-velocity at $t = 0.001$. The results prove that the new method has third-order accuracy. One should note that this test case is unsteady, the numerical accuracy is under the influence of both the temporal order and the spatial order. Here we use a constant CFL number 0.1. If the temporal order is under third-order, it would play the main role on the numerical accuracy when the mesh size is small enough, for example $h = 0.0125$. The results indicates that both the spatial order and the temporal order can achieve about third-order leading to the final third-order shown in Table 1.

3.2 Flow around NACA0012

The flow around NACA0012 with a zero attack angle is used here to test the CPU time. The chord length is 1 m, the far field temperature is 300 K, the density is 1 kg/m^3, and the inlet Mach number is 0.2. Reynolds number based on the inlet parameter and chord length is 1000. The number of elements is 16,826, and the mesh is refined around the airfoil. Figures 3 and 4 show the comparison for our previous method with third-order flux scheme and the method presented in this paper. The results are coincident with each other. A workstation with Intel(R) Xeon(R) CPU E5-2630 V4 @ 2.2GHz 2.2 GHz is used for the calculation, and six cores are employed. Figure 5 shows the convergence history and Table 2 shows the averaged CPU time cost for each time step (10,000 steps). We can see that the method in this paper has relatively lower CPU cost (about 6% less) than our pervious method, while the results are agreed well with each other.

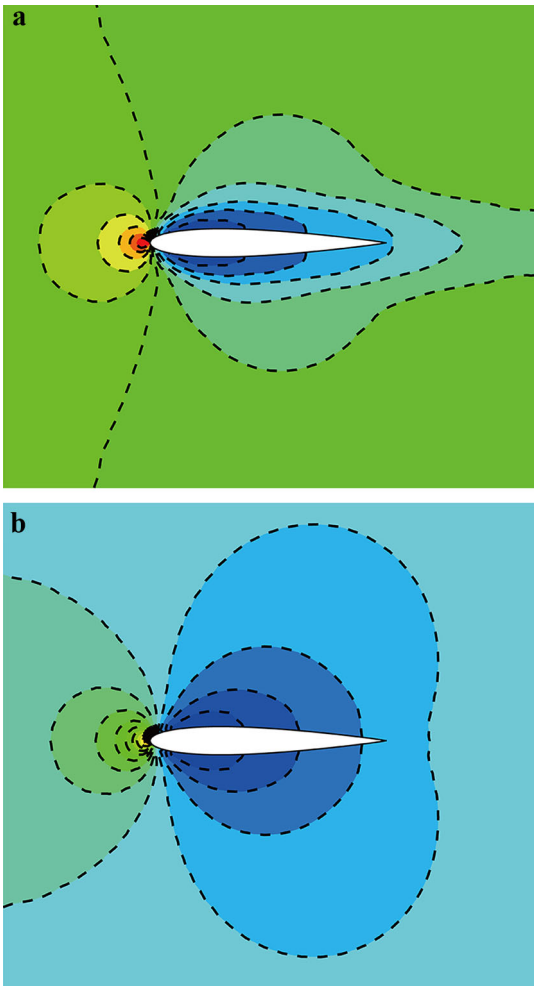

Fig. 3 **a** Density contours and **b** pressure contours. Flood is for third-order flux scheme. *Dashed line* is for second-order flux scheme with the two-stage temporal discretization

3.3 Hypersonic laminar flow past a circular cylinder

In this section, a hypersonic laminar flow problem is used to check the capacity of the method in the hypersonic regime. For the traditional Riemann solver, shock instability is present, called the carbuncle phenomenon. To deal with this problem generally, some cures should be done. In our previous study [18], the results have shown that the flux scheme based on the gas-kinetic theory can prevent the shock instability without any special treatment. Here we employ it again to check the method in this paper. The experiment has been done by Wieting [23]. The far field flow condition is set to be $M_\infty = 8.03$, $T_\infty = 124.94$ K, and the cylinder temperature is $T_W = 294.44$ K. The cylinder radius is cho-

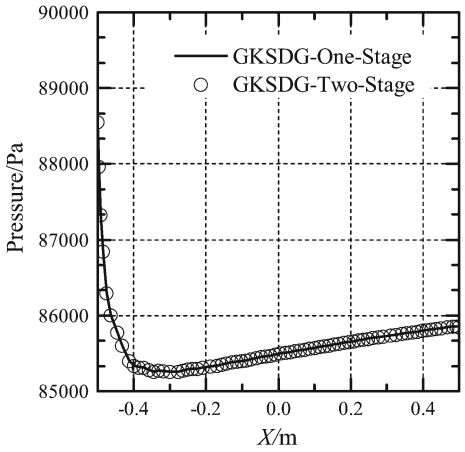

Fig. 4 Comparison of the pressure distribution along the airfoil upper surface

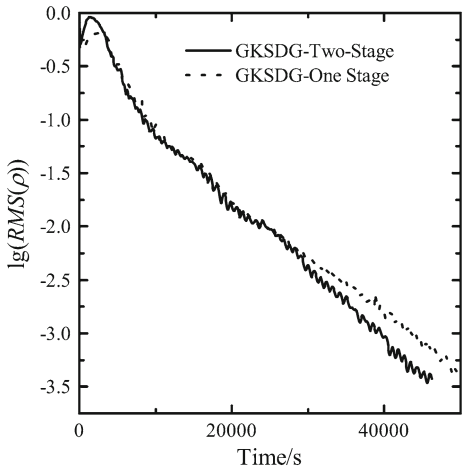

Fig. 5 Comparison of the convergence history

Table 2 Averaged CPU time cost comparison

	GKSDG-one-stage (third-order flux scheme)	GKSDG-two-stage (second-order flux scheme)
CPU time (s)	0.734	0.692

sen as the characteristic length and the Reynolds number is $R_e = 1.835 \times 10^5$ based on the far field flow condition. Figure 6 shows the contours of the pressure and temperature, and the shock instability is not present. The static pressure and heat flux distributions along the cylindrical surface are compared with the experimental data, Fig. 7, they are in good agreement.

3.4 Viscous shock tube

This case is employed to check the capacity of the method for viscous flows [24]. The initial gas is static in the domain

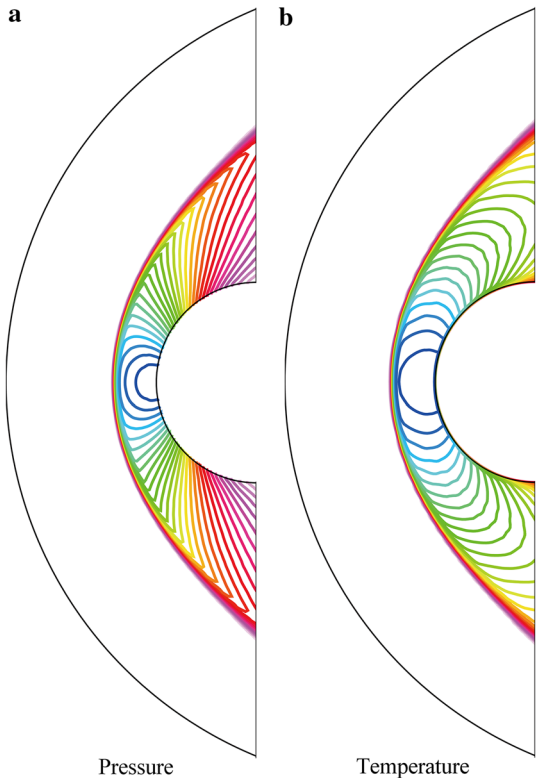

Fig. 6 Pressure and temperature contours (GKSDG-Two-Stage). **a** Pressure. **b** Temperature

$[0, 1] \times [0, 0.5] \times [0, 0.1] \subset \mathbb{R}^3$. A membrane located at $x = 0.5$ and the initial gas states in different sides are

$$(\rho,\ U,\ V,\ W,\ p) = \begin{cases} (120,\ 0,\ 0,\ 0,\ 120/\gamma), & 0 \leqslant x \leqslant 0.5, \\ (1.2,\ 0,\ 0,\ 0,\ 1.2/\gamma), & 0.5 \leqslant x \leqslant 1. \end{cases} \tag{27}$$

The Reynolds number is 200. At $t = 0$, the membrane is removed, and the shock wave moves to the right side with a Mach number $Ma = 2.37$ and reflects at the right endwall. The interaction between the shock wave and the contact discontinuity will be presented. In addition, the bottom boundary in y direction is nonslip adiabatic wall, thus these waves also interact with the horizontal wall and create a thin boundary layer. Here a symmetrical condition is used on the top boundary in the y direction and both boundaries in the z direction. As shown in Fig. 8, the mesh size in the right region is smaller than the one in the left region in x direction due to complex flow phenomena presented on the right side. The density contours at $t = 1.0$ are shown in Fig. 9, and the height of primary vortex predicted by the current method agree well with the reference data [25] as shown in Table 3.

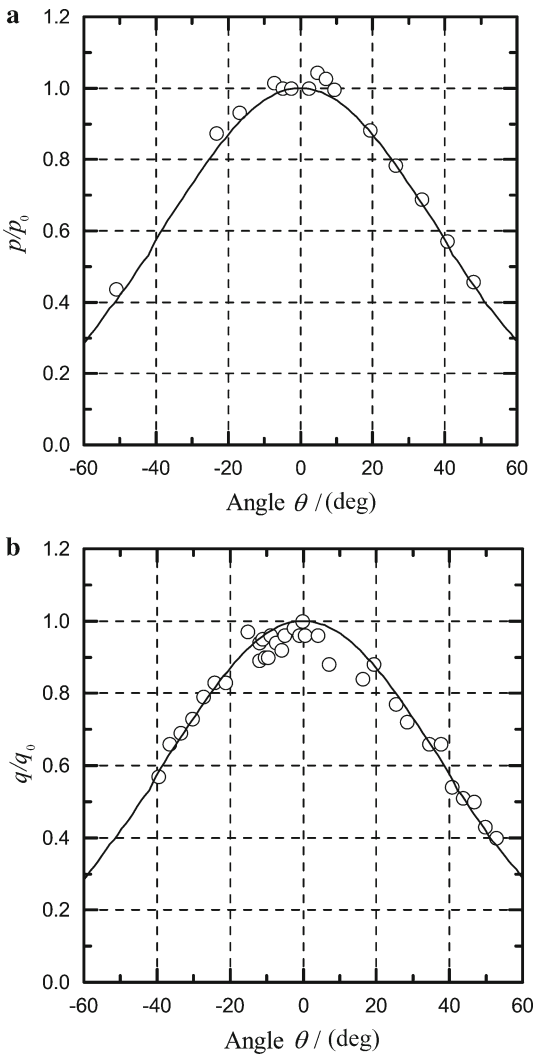

Fig. 7 The static pressure and the heat flux distributions along the cylindrical surface. The *solid line* stands for numerical results. The circle stands for experimental data. **a** Pressure. **b** Heat flux

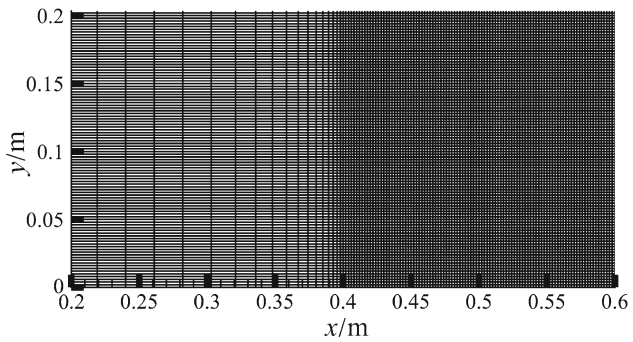

Fig. 8 Mesh used for the viscous shock tube

3.5 3D lid-driven cavity flows

The test cases are also employed to check the capacity of the method for viscous flow. A 3D unit cube with a moving tip is computational domain. The tip moving velocity is $U = 1$ and the non-slip boundary condition is imposed on the tip. Initially, the air in the cube is static, then the tip velocity generates vorticity that propagates throughout the domain. Finally, the flow field reaches a steady state when the Reynolds number is not too large. Here we take three Reynolds numbers: 100, 400, and 1000. The Mach number is set to be 0.3. In order to reduce the CPU cost, a non-uniform Cartesian mesh is selected as in Ref. [18]. The results are compared with the data in Refs. [26,27], as shown in Fig. 10. It indicates that the numerical in this paper a coarser grid are in good agreement with the data from Refs. [26,27], which means the method in this paper has a good capacity for the low-speed viscous flow.

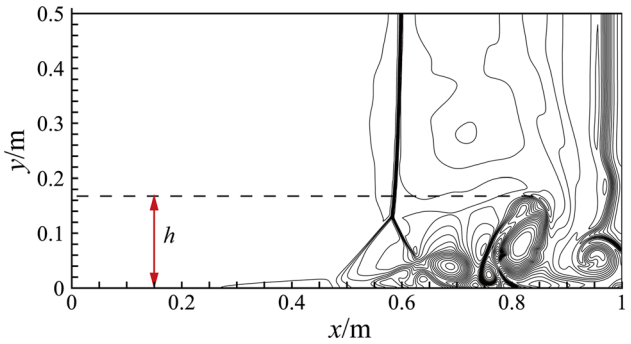

Fig. 9 Density contours for the viscous shock tube problem at $t = 1.0$

Table 3 Comparison of the height of primary vortex

	Method		
	AUSMPW+	M-AUSMPW+	GKSDG-Two-Stage
h	0.163	0.168	0.168

4 Conclusions

A gas-kinetic theory based multidimensional high-order method for the compressible NS solutions has been proposed in this paper. The second-order gas-kinetic flux scheme is employed to estimate fluxes both inside the cell and on the cell interface. Compared with the third-order gas-kinetic flux scheme in our previous study, the second-order scheme is quite simple and easy for using. A two stage temporal discretization is adopted here for maintaining its temporal accuracy. Flow around NACA0012 airfoil is used to check the CPU cost and the result shows the method has lower CPU cost than our previous method, which uses the third-order gas-kinetic flux scheme. Furthermore, several tests cases, including compressible and incompressible

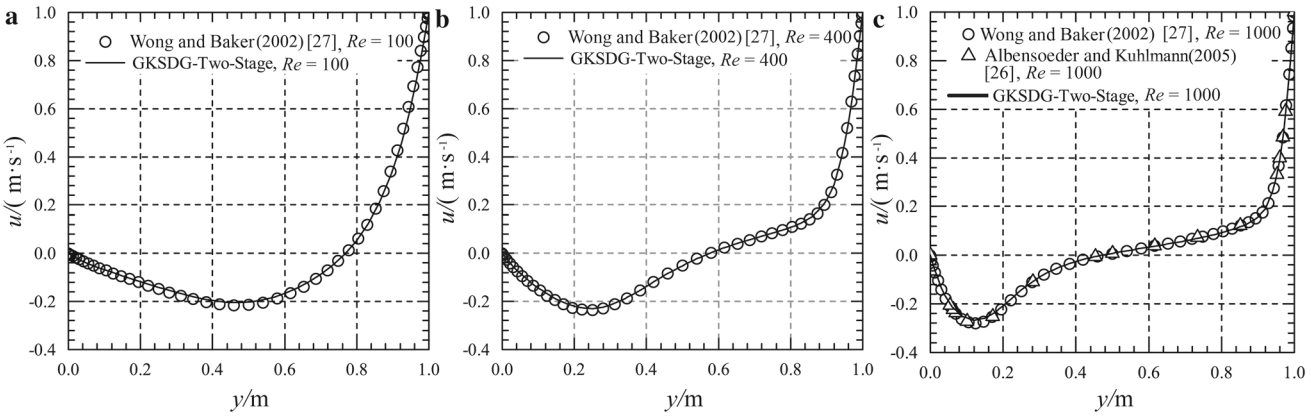

Fig. 10 Comparison of the velocity u along the line ($x = 0,\ 0 \leqslant y \leqslant 1,\ z = 0$)

flow problems, are considered. The results demonstrate its capacity.

Acknowledgements The current work is supported by HKUST research fund PROVOST 13SC01.

References

1. Cockburn, B., Shu, C.-W.: The Runge-Kutta discontinuous Galerkin method for conservation laws V. J. Comput. Phys. **141**, 199–224 (1998)
2. Reed, W.H., Hill, T.: Triangular mesh methods for the neutron transport equation. Los Alamos Report LA-UR-73-479 (1973)
3. Lasaint, P., Raviart, P.A.: On a finite element method for solving the neutron transport equation. Math. Asp. Finite Elem. Partial Differ. Equ. **S4**, 89–123 (1974)
4. Chavent, G., Salzano, G.: A finite-element method for the 1-D water flooding problem with gravity. J. Comput. Phys. **45**, 307–344 (1982)
5. Cockburn, B., Shu, C.-W.: TVB Runge–Kutta local projection discontinuous Galerkin finite element method for conservation laws II. General framework. Math. Comput. **52**, 411–435 (1989)
6. Xu, Y., Shu, C.-W.: Local discontinuous Galerkin methods for high-order time-dependent partial differential equations. Commun. Comput. Phys. **7**, 1–46 (2010)
7. Bassi, F., Rebay, S.: A high-order accurate discontinuous finite element method for the numerical solution of the compressible Navier–Stokes equations. J. Comput. Phys. **131**, 267–279 (1997)
8. Cockburn, B., Shu, C.W.: The local discontinuous Galerkin method for time-dependent convection-diffusion systems. Siam J. Numer. Anal. **35**, 2440–2463 (1998)
9. Kim, S.S., Kim, C., Rho, O.H., et al.: Cures for the shock instability: development of a shock-stable Roe scheme. J. Comput. Phys. **185**, 342–374 (2003)
10. Ren, X.D., Gu, C.W., Li, X.S.: Role of the momentum interpolation mechanism of the Roe scheme in shock instability. https://arxiv.org/vc/arxiv/papers/1509/1509.02776v1.pdf (2016)
11. Li, X.-S., Gu, C.-W.: Mechanism of Roe-type schemes for all-speed flows and its application. Comput. Fluids **86**, 56–70 (2013)
12. Li, X.-S.: Uniform algorithm for all-speed shock-capturing schemes. Int. J. Comput. Fluid Dyn. **28**, 329–338 (2014)
13. Xu, K.: A gas-kinetic BGK scheme for the Navier-Stokes equations and its connection with artificial dissipation and Godunov method. J. Comput. Phys. **171**, 289–335 (2001)
14. Xu, K.: Discontinuous Galerkin BGK method for viscous flow equations: One-dimensional systems. Siam J. Sci. Comput. **25**, 1941–1963 (2004)
15. Liu, H., Xu, K.: A Runge–Kutta discontinuous Galerkin method for viscous flow equations. J. Comput. Phys. **224**, 1223–1242 (2007)
16. Ni, G., Jiang, S., Xu, K.: A DGBGK scheme based on WENO limiters for viscous and inviscid flows. J. Comput. Phys. **227**, 5799–5815 (2008)
17. Luo, H., Luo, L.Q., Xu, K.: A discontinuous Galerkin method based on a BGK scheme for the Navier–Stokes equations on arbitrary grids. Adv. Appl. Math. Mech. **1**, 301–318 (2009)
18. Ren, X., Xu, K., Shyy, W., et al.: A multi-dimensional high-order discontinuous Galerkin method based on gas kinetic theory for viscous flow computations. J. Comput. Phys. **292**, 176–193 (2015)
19. Pan, L., Xu, K., Li, Q., et al.: An efficient and accurate two-stage fourth-order gas-kinetic scheme for the Euler and Navier–Stokes equations. J. Comput. Phys. **326**, 197–221 (2016)
20. Luo, H., Baum, J.D., Löhner, R.: A discontinuous Galerkin method based on a Taylor basis for the compressible flows on arbitrary grids. J. Comput. Phys. **227**, 8875–8893 (2008)
21. Luo, J., Xu, K.: A high-order multidimensional gas-kinetic scheme for hydrodynamic equations. Sci. China Technol. Sci. **56**, 2370–2384 (2013)
22. Guo, Z., Xu, K., Wang, R.: Discrete unified gas kinetic scheme for all Knudsen number flows: low-speed isothermal case. Phys. Rev. E **88**, 033305 (2013)
23. Wieting, A.R.: Experimental study of shock wave interface heating on a cylindrical leading edge. NASA-TM-100484 (1987)
24. Daru, V., Tenaud, C.: High order one-step monotonicity-preserving schemes for unsteady compressible flow calculations. J. Comput. Phys. **193**, 563–594 (2004)
25. Kim, K.H., Kim, C.: Accurate, efficient and monotonic numerical methods for multi-dimensional compressible flows: part II: multi-dimensional limiting process. J. Comput. Phys. **208**, 570–615 (2005)
26. Albensoeder, S., Kuhlmann, H.C.: Accurate three-dimensional lid-driven cavity flow. J. Comput. Phys **206**, 536–558 (2005)
27. Wong, K.L., Baker, A.J.: A 3D incompressible Navier–Stokes velocity–vorticity weak form finite element algorithm. Int. J. Numer. Methods Fluids **38**, 99–123 (2002)